Frontiers of Information Technology & Electronic Engineering
www.jzus.zju.edu.cn; engineering.cae.cn; www.springerlink.com
ISSN 2095-9184 (print); ISSN 2095-9230 (online)
E-mail: jzus@zju.edu.cn

Joint compressed sensing imaging and phase adjustment via an iterative method for multistatic passive radar*

Jue WANG†, Jun WANG

National Laboratory of Radar Signal Processing, Xidian University, Xi'an 710071, China

†E-mail: xdwangjue@163.com

Received Sept. 13, 2016; Revision accepted Jan. 23, 2017; Crosschecked Apr. 12, 2018

Abstract: The resolution of the multistatic passive radar imaging system (MPRIS) is poor due to the narrow bandwidth of the signal transmitted by illuminators of opportunity. Moreover, the inaccuracies caused by the inaccurate tracking system or the error position measurement of illuminators or receivers can deteriorate the quality of an image. To improve the performance of an MPRIS, an imaging method based on the tomographic imaging principle is presented. Then the compressed sensing technique is extended to the MPRIS to realize high-resolution imaging. Furthermore, a phase correction technique is developed for compensating for phase errors in an MPRIS. Phase errors can be estimated by iteratively solving an equation that is derived by minimizing the mean recovery error of the reconstructed image based on the principle of fixed-point iteration technique. The technique is nonparametric and can be used to estimate phase errors of any form. The effectiveness and convergence of the technique are confirmed by numerical simulations.

Key words: Multistatic passive radar; Compressed sensing; Phase adjustment; Fixed-point iteration technique
https://doi.org/10.1631/FITEE.1601423 **CLC number:** TN95

1 Introduction

The conventional synthetic aperture radar (SAR) is monostatic with collocated transmit and receive antenna elements. It is a remote sensing system that can provide high-resolution imagery of target scenes independent of weather and time. Thus, it is widely used in both civil and military installations. The resolution of an SAR is determined by the bandwidth of the signal and the aperture size of the antenna. An alternative approach is imaging with a multistatic configuration where transmit and receive antenna elements are distributed around the target to be imaged. High resolution can be achieved because of the spatial distribution and the frequency diversity provided by the multistatic configuration (Stojanovic et al., 2013). In this study, a multistatic configuration is composed of illuminators of opportunity (such as frequency modulation (FM) stations, television stations, and satellites) and multiple receivers. Because the illuminators are non-cooperative, the configuration presented here is also called the 'multistatic passive radar'. It has advantages over traditional imaging systems because of its low cost, strong survivability, and robustness against deliberate interference (Liu et al., 2014; Lv et al., 2015). On the other hand, a multistatic passive radar system has some limitations. Restricted by the narrow bandwidth of signals (the bandwidth of the radiated signals usually ranges from 100 kHz to 10 MHz) transmitted by the illuminators of opportunity, the resolution of the multistatic passive radar imaging system (MPRIS) is poor. Furthermore, the number of illuminators of opportunity that can be used to observe the target is small.

---

* Project supported by the National Natural Science Foundation of China (No. 61401526), the Innovative Research Team in University, China (No. IRT0954), and the Foundation of National Ministries, China (No. 9140A07020614DZ01)

ORCID: Jue WANG, http://orcid.org/0000-0003-1717-6750

Therefore, the Fourier measurement coverage is relatively sparse, failing to realize high-resolution imaging. To improve the performance of an MPRIS, Wang et al. (2006) proposed a sub-aperture method based on the polar format algorithm. By synthesizing all the sub-apertures formed by transmitters and receivers into a large equivalent aperture, a high-resolution image can be achieved. The principle of the imaging algorithm is similar to tomographic ones and the resolution cell can reach as high as $\lambda/3$ in theory, where λ represents the wavelength of the transmitted signal. However, the sidelobes around the scatterers are relatively high compared with traditional ones, which can be seen from their point-spread function (PSF). The profile of the PSF is a curve that obeys the first kind zero-order Bessel function and the sidelobe is 7.9 dB below the main lobe of the PSF, while the profile of the target response function of the traditional SAR/inverse SAR (ISAR) is a curve that obeys the sinc function and the sidelobe is 13.2 dB below the main lobe. The quality of the image suffers from high sidelobes. To mitigate the influence of high sidelobes, we extend the compressed sensing (CS) technique to a multistatic configuration.

The imaging process can be seen as a process of finding the solution to an inverse problem in imaging (Kirsch, 2011). The precision of the solution is determined by the accuracy of the mathematical model of the observation process. However, the mathematical model often contains errors and uncertainties due to the inaccurate knowledge of both motion of the target and multistatic geometry. The errors will cause a defocus of the reconstructed image. Therefore, techniques for removing the phase errors caused by the inaccurate observation, which are also called ‘autofocusing techniques’ should be developed to improve the quality of the image. Many studies have been carried out with an emphasis on autofocus problems (Brisken et al., 2012, 2014; Giusti et al., 2013). There are mainly two types of autofocusing techniques (Berizzi et al., 2004): one is parametric autofocusing technique, and the typical ones are image entropy based techniques (IEBTs) and image contrast based techniques (ICBTs). The phase error is approximated as a polynomial of high order. By focusing the image based on image quality measurement, the coefficients of the polynomial of different orders can be found and thus the estimate of the phase error is obtained. The image quality measurement can be chosen as an entropy function or an image contrast function (Berizzi and Corsini, 1996; Brisken and Martella, 2014). However, there are various kinds of phase errors in reality and some phase errors cannot be simply approximated as a polynomial. For example, phase errors are slowly arising because of the inaccurate knowledge of the positions of the geometry of the multistatic configuration, while phase errors induced by propagation effects are much more irregular (such as random phase errors) (Önhon and Çetin, 2012). When the form of phase errors in practice does not fit that of the model as assumed, the performance of the autofocusing technique suffers from degradation. Another technique is the nonparametric autofocusing technique. The most well-known ones are phase gradient autofocus (PGA) and prominent point processing (PPP). To perform PGA/PPP well, the following two assumptions should be satisfied: (1) the image can be obtained by applying the Fourier transform on the data after range alignment; (2) phase errors exist only in the azimuth dimension. However, the image domain is reconstructed by the convolution of the data acquired by the multistatic configuration with the function built up based on the scenery to be imaged. Moreover, the resolution parameters used to measure the performance of an MPRIS are chosen in directions of x-axis and y-axis according to the coordinates that were built, and phase errors may exist in both dimensions. Therefore, neither of the conditions is satisfied and the conventional nonparametric autofocusing techniques (PGA/PPP) cannot be used in an MPRIS effectively. In this study, we propose an autofocusing technique that can perform well in an MPRIS. The phase errors can be estimated by iteratively solving an equation derived from minimizing the mean recovery error (MRE) of the reflectivity of the target to be imaged. The proposed method does not assume the form of phase errors, and thus it can be used to estimate phase errors of any form.

2 Geometry of the multistatic passive radar imaging system and high-resolution imaging technique

The geometry under consideration for an MPRIS consists of multiple receivers and a single illuminator because the number of illuminators of opportunity used in reality is usually small. The signal transmitted by an illuminator of opportunity located at $\boldsymbol{r}_\mathrm{t}=(x_\mathrm{t}, y_\mathrm{t})^\mathrm{T}$ is denoted as $s(t)\exp(\mathrm{j}2\pi f_\mathrm{c}t)$, where $s(t)$ is the baseband waveform of the transmitted signal and f_c represents the carrier frequency. The target echo received by the m^th receiver, located at $\boldsymbol{r}_m=(x_m, y_m)^\mathrm{T}$, reflected from the scatterer of the target which is located at $\boldsymbol{r}=(x, y)^\mathrm{T}$, can be given as

$$\gamma_m(t)=\sigma(\boldsymbol{r})s(t-\tau_m(\boldsymbol{r}))\exp[\mathrm{j}2\pi f_\mathrm{c}(t-\tau_m(\boldsymbol{r}))], \quad (1)$$

where $\sigma(\boldsymbol{r})$ is the reflectivity of the scatterer, and $\tau_m(\boldsymbol{r})$ is the propagation delay from the illuminator to the scatterer and back from the scatterer to the m^th receiver, satisfying

$$\tau_m(\boldsymbol{r})=(\|\boldsymbol{r}_t-\boldsymbol{r}\|_2+\|\boldsymbol{r}_m-\boldsymbol{r}\|_2)/c, \quad (2)$$

where c is the velocity of light.

Assume that the distance between the target and stations is much greater than the size of the target usually held in practice. Thus, we can make the following approximations:

$$\begin{cases}\|\boldsymbol{r}_\mathrm{t}-\boldsymbol{r}\|_2\approx\|\boldsymbol{r}_\mathrm{t}\|_2-\boldsymbol{b}_\mathrm{t}^\mathrm{T}\boldsymbol{r},\\ \|\boldsymbol{r}_m-\boldsymbol{r}\|_2\approx\|\boldsymbol{r}_m\|_2-\boldsymbol{b}_m^\mathrm{T}\boldsymbol{r},\end{cases} \quad (3)$$

where $\boldsymbol{b}_\mathrm{t}=\boldsymbol{r}_\mathrm{t}/\|\boldsymbol{r}_\mathrm{t}\|_2$ and $\boldsymbol{b}_m=\boldsymbol{r}_m/\|\boldsymbol{r}_m\|_2$ are unit vectors in the directions of the illuminator and the m^th receiver, respectively. The overall target echo reflected from the entire ground patch to be imaged can be modeled as a superposition of the returns from all scatterers (the target is assumed to consist of several strong scatterers in this study and it is reasonable in reality). The signal received after baseband processing is given as

$$\gamma_m(t)=\int_{\|\boldsymbol{r}\|_2\in\Omega}\sigma(\boldsymbol{r})s(t-\tau_m(\boldsymbol{r}))\,\mathrm{e}^{-\mathrm{j}2\pi f_\mathrm{c}\tau_m(\boldsymbol{r})}\,\mathrm{d}\boldsymbol{r}, \quad (4)$$

where $\tau_m(\boldsymbol{r})\approx(\|\boldsymbol{r}_\mathrm{t}\|_2+\|\boldsymbol{r}_m\|_2)/c-(\boldsymbol{b}_\mathrm{t}+\boldsymbol{b}_m)^\mathrm{T}\boldsymbol{r}/c$ and Ω is the spatial domain of the target region where the function is defined. From Eq. (4), we can easily obtain $\exp[-\mathrm{j}2\pi f_\mathrm{c}(\|\boldsymbol{r}_\mathrm{t}\|_2+\|\boldsymbol{r}_m\|_2)/c]$ contained in the received signal, which does not contribute to the imaging and should be estimated and removed with accuracy. The process to remove the phase term is also called 'translation compensation'. When translation compensation is performed accurately, the imaging system turns into a turntable model. The simplified 2D geometry of an MPRIS is shown in Fig. 1. The Cartesian coordinates are built with the target center as its origin. The illuminator is located right on the x-axis and multiple receivers are distributed around the target region to be imaged. From the viewpoint of the synthetic aperture (Mensa et al., 1980), the rotation of the target could be equivalent to the rotation of the receivers. Therefore, multiple arc sub-apertures whose centers are just the rotation center of the target are synthesized. A large aperture is formed by combining all the sub-apertures. When the aperture consisting of all the sub-apertures subtends an angle equal to 2π, the target can be observed from every aspect angle and thus the system achieves its best performance.

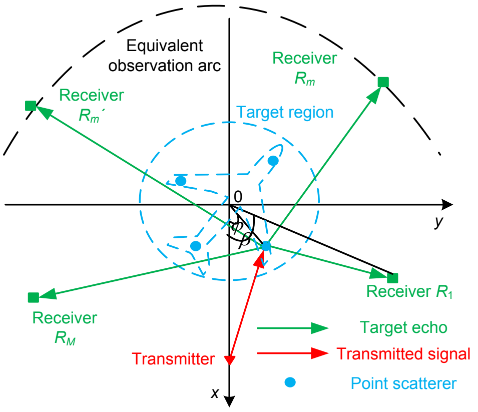

Fig. 1 2D geometry of the multistatic passive radar imaging system (References to color refer to the online version of this figure)

Yarman et al. (2010) proposed that the narrowband signals transmitted by the illuminator of opportunity (such as radio and TV stations) can be denoted as single frequency waveforms. Therefore, after translation compensation, Eq. (4) can be rewritten as

$$\gamma_m(\boldsymbol{k}_m)=\int_{\|\boldsymbol{r}\|_2\in\Omega}\sigma(\boldsymbol{r})\exp(\mathrm{j}\boldsymbol{k}_m^\mathrm{T}\boldsymbol{r})\mathrm{d}\boldsymbol{r}, \quad (5)$$

where $\boldsymbol{k}_m=2\pi(\boldsymbol{b}_t+\boldsymbol{b}_m)/\lambda$ depends on the spatial distribution of the receivers. From Eq. (5), it is obvious that the acquired MPRIS data is the Fourier $\boldsymbol{k}$-space measurement of the underlying spatial reflectivity field. If the Fourier $\boldsymbol{k}$-space measurements fall on a rectangular grid uniformly and densely, the imagery of the target can be obtained by a direct inverse Fourier transform. However, the Fourier $\boldsymbol{k}$-space measurements are distributed sparsely on a circle with radius $1/\lambda$ in the case of an MPRIS consisting of a single illuminator and multiple receivers. No matter how well the interpolation performs, serious interpolation errors would be introduced, resulting in the degeneracy of the resolution of the image. Furthermore, the non-uniform nature of the Fourier $\boldsymbol{k}$-space coverage would aggravate the interpolation errors. The problem can be solved well by the modified polar format algorithm based on the principle of the sub-aperture imaging technique proposed by Wang et al. (2006). However, the performance of the method is restricted by high sidelobes, which are only 7.9 dB below the main lobe even when the equivalent aperture subtends an angle 2π. Therefore, the PSF is chosen as the metric to measure the performance of the imaging system. PSF is an important criterion for evaluating the imaging performance of a radar system, which can be used to represent the capability of a system to separate two close points. Based on the reciprocity theorem (Gonzalez-Valdes et al., 2014), the PSF of the system can be derived as

$$h(\boldsymbol{r})=\sum\nolimits_m \exp(-\mathrm{j}\boldsymbol{k}_m^{\mathrm{T}}\boldsymbol{r}). \tag{6}$$

Fig. 2 shows different PSFs for different multistatic configurations. The carrier frequency of the transmitted signal is adopted as 600 MHz. Suppose that 12 receivers are distributed around the target uniformly, and the aspect angle of receivers noted as R_m (m=1, 2, …, M, and m represents the index of receivers) ranges from 0 to 2π. Limited by various external conditions (such as the geometry of the multistatic configuration), some receivers may not perform well, and thus some sub-apertures cannot be formed in practice; that is to say, there are gaps among the equivalent sub-apertures. Assume that there are M sub-apertures for a target consisting of the full equivalent aperture. Fig. 2a shows the geometry of the sub-apertures noted as S_m (m=1, 2, ..., M). The realistic PSF, when all sub-apertures are synthesized effectively and the equivalent aperture subtends an angle equal to 2π, is given in Fig. 2b. Figs. 2c and 2d represent PSFs of the multistatic configuration when the data acquired by sub-apertures S_{10}–S_{12} and S_7–S_{12} are missing, respectively.

The plots have been normalized to the maximum amplitude. Figs. 2b–2d show that the main lobe of the PSF is broadening with the decrease in the number of sub-apertures, while the relative sidelobe level becomes higher. Therefore, the performance of the imaging system is subjected to degradation with the decrease in the sub-apertures. Recently, theory developed in CS can be used to recover the sparse imagery with a limited number of measurements due to the discontinuities of the sub-apertures, by exploiting the sparsity of the signal to be recovered. Consider the image formation of the target scenes consisting of a set of point reflectors. The geometry of the multistatic configuration is shown in Fig. 1. By discretizing Eq. (5), the imaging model for an MPRIS can be derived as

$$\boldsymbol{\gamma}=\boldsymbol{A}\boldsymbol{\sigma}, \tag{7}$$

where vector $\boldsymbol{\gamma}$ represents the observed set of signals received by all receivers, which can be used to form sub-apertures. Assume that there are P effective sub-apertures in all; thus, $\boldsymbol{\gamma}$ can be denoted as $\boldsymbol{\gamma}=[\gamma_1, \gamma_2, \ldots, \gamma_P]^{\mathrm{T}}$, where $P \le M$ (M is the total number of receivers). Assume that the sampling measurements acquired by each of the sub-apertures are L_0; thus, the data set observed by the p^{th} (p=1, 2, ..., P) sub-aperture can be denoted as $\boldsymbol{\gamma}_p=[\gamma_{(p-1)L_0+1}, \ldots, \gamma_{pL_0}]^{\mathrm{T}}$. γ_l represents the arbitrary sample measurement of the valid data set in the target echo, where l belongs to the set $\{l|1\le l\le L_0\cdot P\}$. $\boldsymbol{\sigma}$ represents the spatial reflectivity of the imagery scene reconstructed in the rectangular grid, $\boldsymbol{\sigma}=[\sigma(x_1, y_1), \sigma(x_1, y_2), \ldots, \sigma(x_q, y_u), \ldots, \sigma(x_Q, y_U)]$ (supposing that there are Q bins in the direction of x-axis and U bins in the direction of y-axis). $\sigma(x_q, y_u)$ is the reflectivity of the point scatterer located at (x_q, y_u) in the coordinates. Matrix $\boldsymbol{A}$ is given as

$$\begin{cases}\boldsymbol{A}(l,:)=[\boldsymbol{a}_l(1,1), \boldsymbol{a}_l(1,2), \ldots, \boldsymbol{a}_l(q,u), \ldots, \boldsymbol{a}_l(Q,U)],\\ \boldsymbol{a}_l(q,u)=\exp[\mathrm{j}2\pi(x_q(1+\cos\beta_l)+y_u\sin\beta_l)/\lambda],\end{cases} \tag{8}$$

where β_l (l=1, 2, …, L_0P) represents the equivalent bistatic angles. Based on the CS theory, when matrix $\boldsymbol{A}$ satisfies the restricted isometry property (RIP), the sparse vector $\boldsymbol{\beta}$ can be reconstructed by solving the

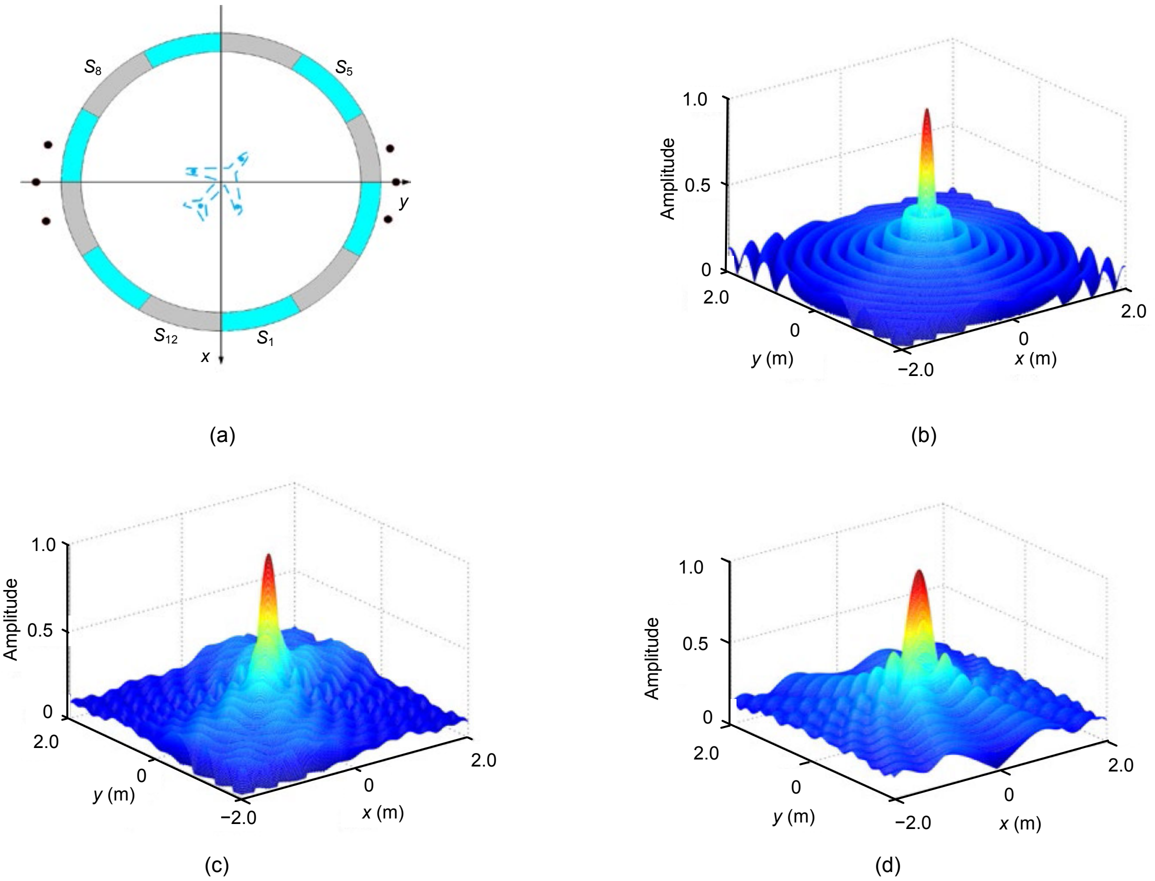

Fig. 2 Geometry of the sub-apertures and point-spread functions (PSFs) for different multistatic configurations: (a) geometry of the sub-apertures; (b) PSFs for full apertures; (c) PSFs in the case of missing sub-apertures S_{10}–S_{12}; (d) PSFs in the case of missing sub-apertures S_7–S_{12} (References to color refer to the online version of this figure)

following optimization problem:

$$\min(\|\boldsymbol{\gamma}\|_0) \quad \text{s.t. } \boldsymbol{\gamma} = \boldsymbol{A\sigma}, \tag{9}$$

where $\|\cdot\|_0$ denotes the l_0 norm and $\min(\cdot)$ the minimization. However, the above optimization problem is essentially a non-deterministic polynomial-time hard (NP-hard) problem. Candès and Tao (2006) and Donoho (2006) demonstrated that the sparse signal can be reconstructed by solving the following convex problem equivalently:

$$\min(\|\boldsymbol{\gamma}\|_1) \quad \text{s.t. } \boldsymbol{\gamma} = \boldsymbol{A\sigma}. \tag{10}$$

In Eq. (10), l_1 norm minimizes most of the elements of $\boldsymbol{\sigma}$ with a few large ones in accordance with the sparsity of spatial reflectivity. The optimization problem can be solved effectively by some CS algorithms and software (Grant et al., 2015). However, the inaccurate knowledge of the positions of illuminators, receivers, and the target would cause phase errors in the target echo, resulting in the degradation of the image quality. Therefore, a nonparametric autofocusing technique is proposed, which can be used to jointly estimate phase errors and reconstruct the high-resolution image. It is noteworthy that although the analysis above is based on the isotropic target model, it does not limit the applicability of the proposed approach to the anisotropic case. The problem of anisotropy can be solved by dividing the entire observation aperture into multiple smaller sub-apertures (Wu et al., 2015). When the observation angle corresponding to each sub-aperture does not vary much, it is reasonable to assume that the scattering coefficients are invariant in each sub-aperture. The positions of the scattering coefficients are the same across different sub-apertures, whereas their values are different. Hence, the multistatic passive radar imaging problem can be regarded as the reconstruction of multiple groups of sparse scattering coefficients. In addition, the nonparametric autofocusing technique proposed in our study can be readily extended to the anisotropic case. Since the positions of the scattering coefficients are the same across different sub-apertures, phase errors can be estimated within each observation aperture with our proposed autofocusing technique. From the above analysis, we can see that the model we propose can be easily extended to an anisotropic case.

3 Autofocusing techniques for multistatic passive radar imaging system

The mathematical imaging model for an MPRIS in the case of existing phase errors can be formulated as

$$\bar{\boldsymbol{\gamma}} = \boldsymbol{\Gamma}\boldsymbol{A}\boldsymbol{\sigma} = \boldsymbol{A}\bar{\boldsymbol{\sigma}}(\phi), \tag{11}$$

where $\bar{\boldsymbol{\gamma}}$ is the target echo contained by phase errors, $\boldsymbol{\Gamma}$ is a diagonal matrix with the phase errors existing on its diagonal line, i.e., $\boldsymbol{\Gamma} = \mathrm{diag}(\mathrm{e}^{\mathrm{j}\phi_1}, \mathrm{e}^{\mathrm{j}\phi_2}, \cdots, \mathrm{e}^{\mathrm{j}\phi_L})$, where $\mathrm{e}^{\mathrm{j}\phi_l}$ (l=1, 2, ..., L, $L=L_0P$) is the phase error of the l^{th} sample measurement in the target echo. $\bar{\boldsymbol{\sigma}}(\phi)$ is the defocused image recovered in the case of phase errors presented in the target echo. The objective of the autofocus technique is to produce phase estimates $\hat{\phi} = \{\hat{\phi}_1, \hat{\phi}_2, \cdots, \hat{\phi}_L\}$ such that the image quality is optimized over a given metric. The criterion we choose here to measure the image quality is the relative recovery error, namely, the MRE for the spatial reflectivity normalized by its energy:

$$e(\phi) = \sqrt{\frac{\|\hat{\boldsymbol{\sigma}}(\phi) - \boldsymbol{\sigma}\|_2^2}{\|\boldsymbol{\sigma}\|_2^2}}, \tag{12}$$

where $\hat{\boldsymbol{\sigma}}(\phi)$ is the estimate of the refocused imagery scenario when phase errors are compensated for by the phase estimates. Phase estimates can be derived from minimizing the MRE. Thus, the estimate of phase errors can be transformed into

$$\hat{\phi} = \arg\min_{\phi} e(\phi). \tag{13}$$

Obviously, the optimization problem (13) is an implicit function with respect to ϕ. There is no closed-form solution for the optimization expression. This problem can be solved well by an iterative method, which is also called the 'fixed-point algorithm' (Wang et al., 2004).

From Eqs. (7) and (11), we can see that the cost function (12) can be equivalently transformed into Eq. (14) since $\|\boldsymbol{A}\boldsymbol{u}\|_2^2 = \|\boldsymbol{u}\|_2^2$ holds for any vector $\boldsymbol{u}$:

$$\begin{aligned} e(\phi) &= \sqrt{\frac{\left\|\boldsymbol{A}\hat{\boldsymbol{\sigma}}(\phi) - \boldsymbol{A}\boldsymbol{\sigma}\right\|_2^2}{\left\|\boldsymbol{A}\boldsymbol{\sigma}\right\|_2^2}} \\ &= \sqrt{\frac{\left\|\boldsymbol{\Gamma}\boldsymbol{A}\boldsymbol{\sigma} - \boldsymbol{\gamma}\right\|_2^2}{\left\|\boldsymbol{\gamma}\right\|_2^2}} \\ &= \sqrt{\frac{\sum_{l=1}^{L}\left\|\exp(\mathrm{j}\phi_l)\boldsymbol{A}(l,:)\boldsymbol{\sigma} - \boldsymbol{\gamma}_l\right\|_2^2}{\left\|\boldsymbol{\gamma}\right\|_2^2}}. \end{aligned} \tag{14}$$

We can see from Eq. (14) that the minimized $e(\phi)$ is equivalent to the minimized $\|e(\phi)\|_2^2$. The necessary condition for the minimization is described by setting the derivative of $\|e(\phi)\|_2^2$ with respect to the parameter ϕ_l as zero, i.e.,

$$\partial\|e(\phi)\|_2^2 \big/ \partial\phi_l = 0, \quad l = 1, 2, \cdots, L. \tag{15}$$

The derivative of $\|e(\phi)\|_2^2$ with respect to the parameter ϕ_l can be obtained from Eq. (14):

$$\begin{aligned} \frac{\partial\left\|e(\phi)\right\|_2^2}{\partial\phi_l} &= \mathrm{j}\begin{bmatrix} \exp(-\mathrm{j}\phi_l)\boldsymbol{\sigma}^{\mathrm{H}}\boldsymbol{A}(l,:)^{\mathrm{H}}\boldsymbol{\gamma}_l \\ -\exp(\mathrm{j}\phi_l)\boldsymbol{\gamma}_l^{\mathrm{H}}\boldsymbol{A}(l,:)\boldsymbol{\sigma} \end{bmatrix} \Bigg/ \left\|\boldsymbol{\gamma}\right\|_2^2 \\ &= -2\frac{\mathrm{Im}(\exp(-\mathrm{j}\phi_l)\boldsymbol{\sigma}^{\mathrm{H}}\boldsymbol{A}(l,:)^{\mathrm{H}}\boldsymbol{\gamma}_l)}{\left\|\boldsymbol{\gamma}\right\|_2^2}, \end{aligned} \tag{16}$$

where $(\cdot)^{\mathrm{H}}$ is the conjugate transposition operator and $\mathrm{Im}(\cdot)$ denotes the imaginary part of the complex value. Substituting Eq. (16) into Eq. (15), we can obtain

$$\phi_l = d\pi + \angle\boldsymbol{\sigma}^{\mathrm{H}}\boldsymbol{A}(l,:)^{\mathrm{H}}\boldsymbol{\gamma}_l, \tag{17}$$

where d represents an arbitrary integer and $\angle\boldsymbol{\sigma}^{\mathrm{H}}\boldsymbol{A}(l,:)^{\mathrm{H}}\boldsymbol{\gamma}_l$ denotes the phases of $\boldsymbol{\sigma}^{\mathrm{H}}\boldsymbol{A}(l,:)^{\mathrm{H}}\boldsymbol{\gamma}_l$.

The estimates of ϕ_l can also be taken as $\phi_l = \angle\boldsymbol{\sigma}^{\mathrm{H}}\boldsymbol{A}(l,:)^{\mathrm{H}}\boldsymbol{\gamma}_l$ for simplicity, which performs well in our test. From Eq. (11), we can see that there is no closed-form solution for ϕ_l because calculating $\angle\boldsymbol{\sigma}^{\mathrm{H}}\boldsymbol{A}(l,:)^{\mathrm{H}}\boldsymbol{\gamma}_l$ requires ϕ_l. We resort to the fixed-point algorithm to solve the optimization problem. A similar approach for range-Doppler (RD) images was considered by Wang et al. (2004). Note that ϕ is initialized as zero and the spatial reflectivity is reconstructed by the CS algorithm described in Section 2 with the target echo contaminated by phase errors. Then the phase errors can be estimated by Eq. (17). The target echo is updated by multiplying the conjugate phase errors, which are found in the previous iteration with the original received signal, i.e., $\hat{\boldsymbol{\gamma}}_u = \hat{\boldsymbol{\Gamma}}^{\mathrm{H}}\overline{\boldsymbol{\gamma}}$, where $\hat{\boldsymbol{\Gamma}} = \mathrm{diag}(\mathrm{e}^{\mathrm{j}\hat{\phi}_1}, \mathrm{e}^{\mathrm{j}\hat{\phi}_2}, \cdots, \mathrm{e}^{\mathrm{j}\hat{\phi}_L})$, $\hat{\phi}_l\ (l = 1, 2, \cdots, L)$ represents phase errors estimated in the previous iteration, and $\hat{\boldsymbol{\gamma}}_u$ represents the updated target echo that is obtained. Again, spatial reflectivity is recovered by CS with the updated received signal. The phase errors can be found by Eq. (17). The iterations described above are carried out round after round until the relative recovery error does not change obviously during adjacent iterations. The halt condition can be directly expressed as

$$e(\hat{\phi}_i) = \sqrt{\|\hat{\boldsymbol{\sigma}}_i - \hat{\boldsymbol{\sigma}}_{i-1}\|_2^2 / \|\hat{\boldsymbol{\sigma}}_{i-1}\|_2^2} \le \varepsilon, \tag{18}$$

where $\hat{\boldsymbol{\sigma}}_i$ and $\hat{\boldsymbol{\sigma}}_{i-1}$ denote the estimates of the spatial reflectivity obtained after the current iteration and the previous iteration, respectively, and ε is a small constant. The convergence of the iteration is easily guaranteed by inequality (18) and the algorithm converges very quickly. An optimal solution can be obtained by the fixed-point algorithm with only several iterations, which will be shown in the following simulations. For clarity, a flowchart for multistatic passive radar imaging is given in Fig. 3.

4 Simulation

In our simulation, 12 receivers (M=12) uniformly located around the imaging scenery are used. The illuminator of opportunity is assumed to locate right on the x-axis. The geometry of the MPRIS is shown in Fig. 1. The carrier frequency of the transmitted signal is 600 MHz. The target is supposed to consist of four isotropic scatterers with the unit reflection coefficient. A model of the imaging scenario whose dimension is 3 m×3 m in the directions of x-axis and y-axis is constructed in Fig. 4.

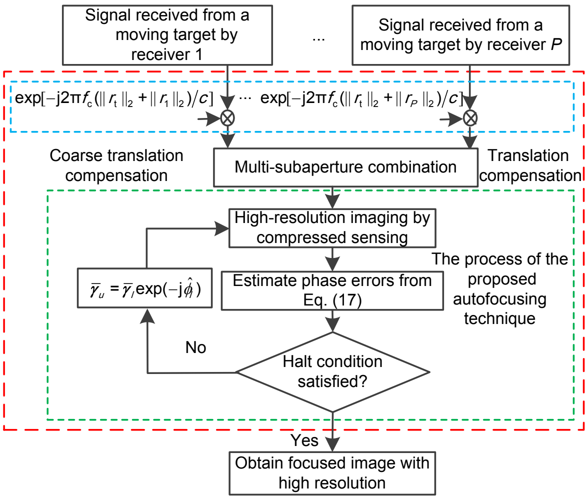

Fig. 3 Flowchart of multistatic passive radar imaging

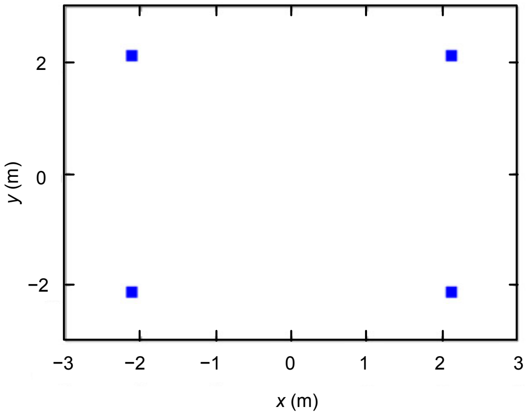

Fig. 4 Model of the imaging scenario

In the ideal case, all receivers can be used to form equivalent sub-apertures around the target effectively. A large complete aperture consisting of all the sub-apertures (i.e., S_1–S_{12}, with the geometry of the sub-apertures shown in Fig. 2a) subtends an angle equal to the processing interval 2π. The resolution in both directions is the best in this case. Fig. 5 shows the imaging results obtained using the polar format algorithm and the CS approach under different sparse sub-apertures patterns. In the following, we extract echoes from the complete aperture data set as the gaped aperture sampling data for the simulation. Figs. 5a–5c show the imaging results with different sparse sub-aperture patterns with different numbers of sub-apertures. Fig. 5a presents the imaging results when all the sub-apertures are available; Fig. 5b shows the imaging results when sub-apertures S_{10}–S_{12} are missing; Fig. 5c shows the imaging results when sub-apertures S_7–S_{12} are missing. The first and third rows are the imaging results obtained using the polar format algorithm and the CS approach, respectively. To show the performance of these approaches more explicitly, the profiles of the images along the y-axis are shown in the second and fourth rows. From

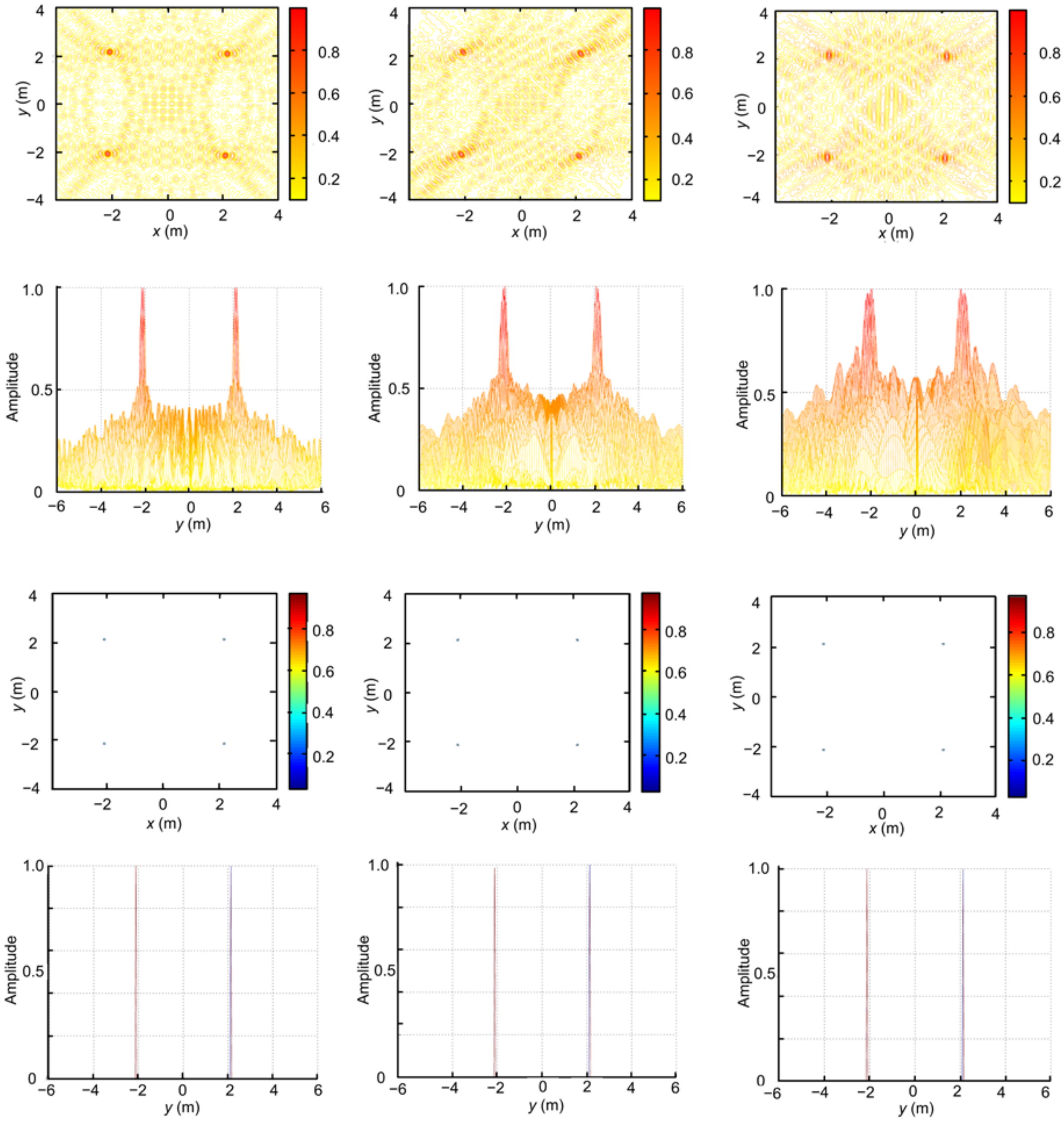

(a) (b) (c)

Fig. 5 Imaging results obtained using the polar format algorithm and compressed sensing: (a) imaging results when all the sub-apertures are available; (b) imaging results when sub-apertures S_{10}–S_{12} are missing; (c) imaging results when sub-apertures S_7–S_{12} are missing (References to color refer to the online version of this figure)

the first and second rows of Fig. 5, we can see that the main lobe in the imaging results is broadening with the decreasing number of sub-apertures, while the sidelobe levels are increasing. This is also in line with the expectation that the performance of the polar algorithm will suffer from degradation given the decreasing coverage of the Fourier measurements. Comparing the third and fourth rows of Fig. 5 with the previous two rows, we can see that the point scatterers of the target can be reconstructed almost without distortion by CS even when half of the aperture data is missing.

From the analysis above, the CS approach is extended to an MPRIS and a high-resolution image is realized. However, high-quality imaging results are obtained based on phase term $\exp[-\mathrm{j}2\pi f_{\mathrm{c}}(\|\boldsymbol{r}_{\mathrm{t}}\|_2+\|\boldsymbol{r}_m\|_2)/c]$, which is accurately compensated for by the process of translation motion compensation. Residual phase errors are unavoidable during this process due to various reasons. Typical reasons would include phase errors caused by the uncertainties of the tracking system, phase errors arising due to propagation effects, and so on. Suppose that a random phase error is distributed in $[0, 2\pi]$. Fig. 6 shows the image results reconstructed by CS without phase error compensation when half of the sub-apertures are missing. The scale of the plots is linear and it has been normalized to its maximum amplitude. The profile of the image along y-axis is shown in Fig. 6b. We can see that the residual phase errors would seriously deteriorate the quality of the reconstructed image. Many virtual point scatters occur in the imaginary scenario, and the target is almost unrecognizable. Thus, further autofocusing is required to compensate for the phase error. Figs. 6c and 6d present the corresponding imaging results with our proposed autofocusing technique. Comparing these results with the imaging results from CS shown in Fig. 5c, we can easily see that the performance of

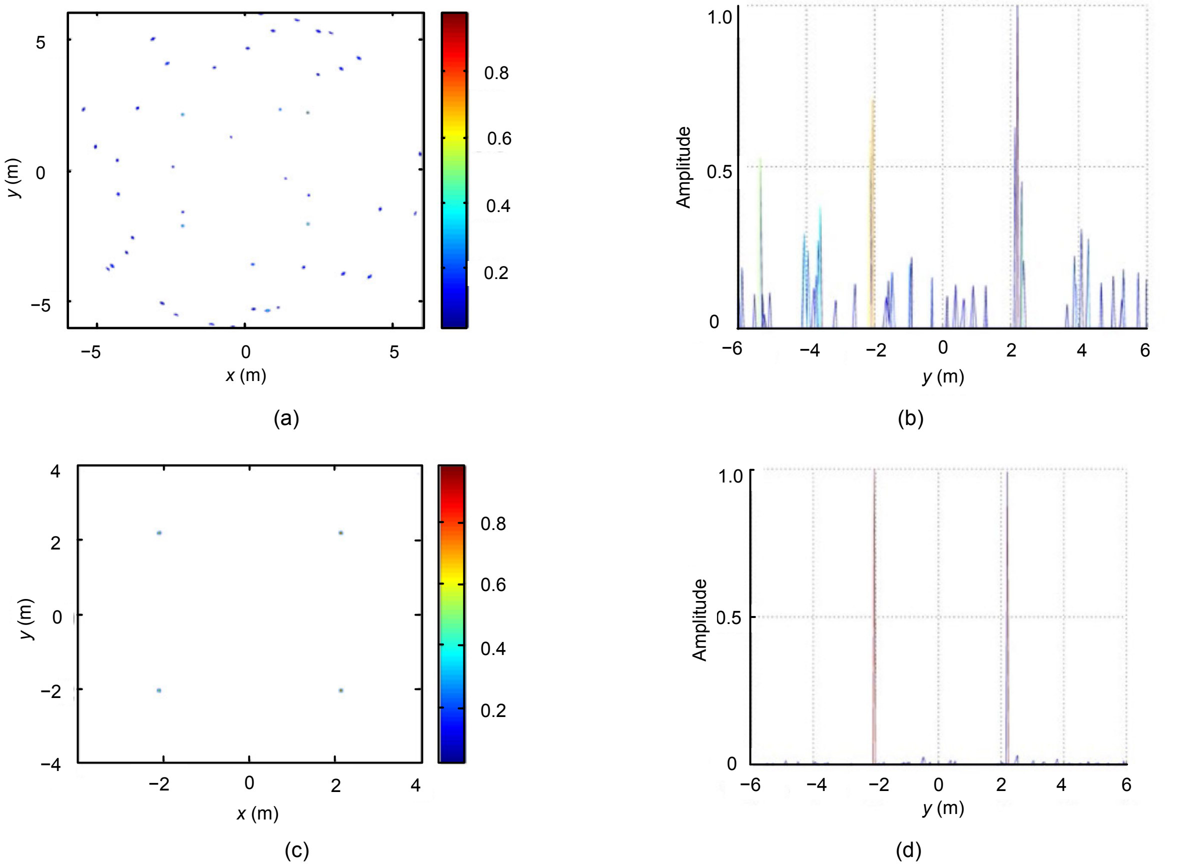

(a) (b)

(c) (d)

Fig. 6 Reconstructed image results before and after using the proposed autofocusing technique: (a) reconstructed image with the phase error; (b) profile of the defocused image; (c) image refocused by the proposed autofocusing technique; (d) profile of the refocused image (References to color refer to the online version of this figure)

the imaging system has been improved significantly after applying the proposed autofocusing technique. Most of the virtual scatterers are mitigated by the autofocusing technique, and the target consisting of several strong scatterers is discernable.

The original phase errors and their estimates are also compared in Fig. 7. The estimates of the phase errors (dashed line) coincide with the real ones (solid line) basically.

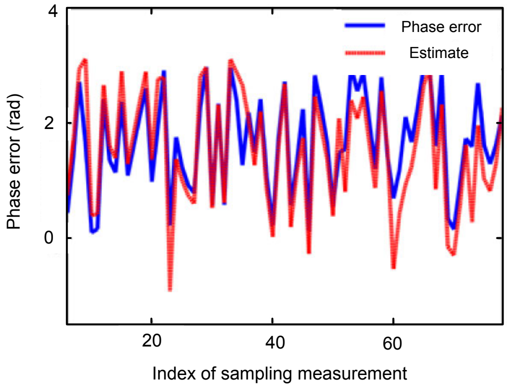

Fig. 7 Comparison of the estimates of phase errors and the true ones

Furthermore, simulations are performed to test the performance of the proposed autofocusing technique with regard to two aspects: convergence of the algorithm and quality of the image. To provide a quantitative evaluation of the two aspects, two metrics are considered here. The first metric can be chosen as the MRE for spatial reflectivity, which is already defined in Eq. (11). Herein, we use image contrast (IC) as the second metric. Image contrast can be used as a suitable measurement to measure the focus quality of an image in SAR/ISAR imaging. The definition of IC is given as

$$C=\sqrt{E[\boldsymbol{\sigma}-E(\boldsymbol{\sigma})]^2}\Big/E(\boldsymbol{\sigma}), \tag{19}$$

where $E(\cdot)$ stands for the expectation operator and $E(\boldsymbol{\sigma})$ represents the spatial mean of the image over the region to which the target belongs. From the definition, it can be found that the function C represents the normalized effective power of image intensity $\boldsymbol{\sigma}$. When the image is defocused, the image intensity levels are concentrated around the mean value and the contrast is low. On the other hand, when the image is well focused, the image contrast will reach its maximum. Both of the metrics presented here are used as quantitative metrics to evaluate the performance of the proposed algorithm. The corresponding simulations are shown in Fig. 8.

Fig. 8a shows the variation in MRE according to the number of iterations. The MRE is the basis on which the adjustment phase is derived. We can see that the MRE reaches its minimum after approximately eight iterations and remains unchanged afterwards. This is equivalent to saying that the proposed iterative algorithm achieves convergence.

The variation in IC according to the number of iterations is given in Fig. 8b. It can be easily seen that the contrast increases with the number of iterations. With the increasing number of iterations, the image quality is basically enhanced. After eight iterations, the value of IC remains unchanged. It validates the effectiveness of the proposed algorithm. In addition, the convergence of the algorithm is confirmed.

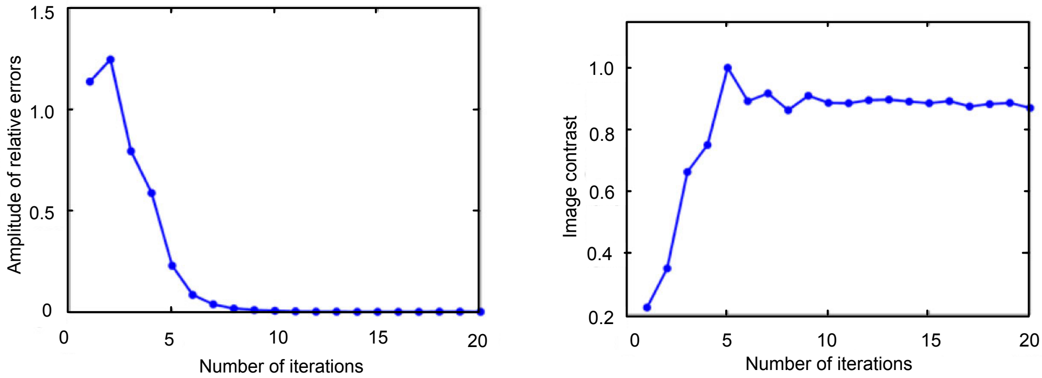

(a) (b)

Fig. 8 Performance of the proposed autofocusing technique: (a) variation in the mean recovery error (MRE) according to the number of iterations; (b) variation in image contrast according to the number of iterations

5 Conclusions

In this paper, an MPRIS has been constructed with a single external illuminator. Since the signal transmitted by the illuminator has a narrow bandwidth and is non-cooperative, we have presented a polar format imaging algorithm to realize high-resolution imaging based on the tomographic principle. Furthermore, a sparsity-driven algorithm has been extended to the MPRIS and a super-resolution image has been obtained even when several sub-apertures are missing. Finally, an autofocusing technique has been developed to improve the performance of the imaging system based on the minimization of the mean relative recovery error of the reconstructed image. The effectiveness of the proposed approach has been manifested in theory and by simulation results. It is noteworthy that phase errors can be compensated for well in the proposed approach when a high signal-to-noise ratio (SNR) gain of the image is achieved. However, the high SNR gain by coherent integration is not achievable in the multistatic passive radar system presented in this study. Therefore, the imaging approach is submerged by strong noise. In a sparsity-driven imaging case, the robustness of the proposed approach can be achieved by modifying the constraint conditions of the cost function, i.e.,

$$\min(\|\boldsymbol{\gamma}\|_1) \ \text{ s.t. } \|\boldsymbol{\gamma}-\boldsymbol{A}\boldsymbol{\sigma}\|_2 \le \varepsilon, \qquad (20)$$

where ε represents the tolerance of the energy of the noise. By solving the l_1 norm optimization problem above, the quality of the image recovered by the passive radar system can be enhanced under a low SNR gain. Due to the scope of this study, the sparsity-driven imaging algorithm, which is robust to noise in the MPRIS, is not presented here. The relevant content will be investigated in our future work.

References

Berizzi F, Corsini G, 1996. Autofocusing of inverse synthetic aperture radar images using contrast optimization. *IEEE Trans Aerosp Electron Syst*, 32(3):1185-1191. https://doi.org/10.1109/7.532282

Berizzi F, Martorella M, Haywood B, et al., 2004. A survey on ISAR autofocusing techniques. Proc Int Conf on Image Processing, p.9-12. https://doi.org/10.1109/ICIP.2004.1418676

Brisken S, Martella M, 2014. Multistatic ISAR autofocus with an image entropy-based technique. *IEEE Aerosp Electron Syst Mag*, 29(7):30-36. https://doi.org/10.1109/MAES.2014.130140

Brisken S, Martorella M, Mathy T, et al., 2012. Multistatic ISAR autofocussing using image contrast optimization. IET Int Conf on Radar Systems, p.1-4. https://doi.org/10.1049/cp.2012.1623

Brisken S, Martorella M, Mathy T, et al., 2014. Motion estimation and imaging with a multistatic ISAR system. *IEEE Trans Aerosp Electron Syst*, 50(3):1701-1714. https://doi.org/10.1109/TAES.2014.130099

Candès EJ, Tao T, 2006. Near-optimal signal recovery from random projections: universal encoding strategies? *IEEE Trans Inform Theory*, 52(12):5406-5425. https://doi.org/10.1109/TIT.2006.885507

Donoho DL, 2006. Compressed sensing. *IEEE Trans Inform Theory*, 52(4):1289-1306. https://doi.org/10.1109/TIT.2006.871582

Giusti E, Tomei S, Bacci A, et al., 2013. Autofocus for CS based ISAR imaging in the presence of gapped data. Proc 2nd Int Workshop on Compressed Sensing Applied to Radar, p.1-4.

Gonzalez-Valdes B, Allan G, Rodriguez-Vaqueiro Y, et al., 2014. Sparse array optimization using simulated annealing and compressed sensing for near-field millimeter wave imaging. *IEEE Trans Antennas Propag*, 62(4): 1716-1722. https://doi.org/10.1109/TAP.2013.2290801

Grant M, 2010. CVX: Matlab Software for Disciplined Convex Programming, Version 1.21. http://cvxr.com/cvx

Kirsch A, 2011. An Introduction to the Mathematical Theory of Inverse Problems. Springer Science & Business Media, New York, NY. https://doi.org/10.1007/978-1-4419-8474-6

Liu J, Li HB, Himed B, 2014. Two target detection algorithms for passive multistatic radar. *IEEE Trans Signal Process*, 62(22):5930-5939. https://doi.org/10.1109/TSP.2014.2359637

Lv XY, Wang J, Wang J, 2015. Robust direction of arrival estimate method in FM-based passive bistatic radar with a four-element Adcock antenna array. *IET Radar Sonar Navig*, 9(4):392-400. https://doi.org/10.1049/iet-rsn.2014.0270

Mensa D, Heidbreder G, Wade G, 1980. Aperture synthesis by object rotation in coherent imaging. *IEEE Trans Nucl Sci*, 27(2):989-998. https://doi.org/10.1109/TNS.1980.4330965

Önhon NÖ, Çetin M, 2012. A sparsity-driven approach for joint SAR imaging and phase error correction. *IEEE Trans Image Process*, 21(4):2075-2088. https://doi.org/10.1109/TIP.2011.2179056

Stojanovic I, Çetin M, Karl WC, 2013. Compressed sensing of monostatic and multistatic SAR. *IEEE Geosci Remote Sens Lett*, 10(6):1444-1448. https://doi.org/10.1109/LGRS.2013.2259794

Wang J, Liu X, Zhou Z, 2004. Minimum-entropy phase adjustment for ISAR. *IEE Proc Radar Sonar Navig*, 151(4):203-209. https://doi.org/10.1049/ip-rsn:20040692

Wang J, Zhang XW, Bao Z, 2006. Passive radar imaging algorithm based on sub-apertures synthesis of multiple television stations. Proc Int Conf on Radar, p.1-4. https://doi.org/10.1109/ICR.2006.343138

Wu QS, Zhang YD, Amin MG, et al., 2015. High-resolution passive SAR imaging exploiting structured Bayesian compressive sensing. *IEEE J Sel Top Signal Process*, 9(8):1484-1497. https://doi.org/10.1109/JSTSP.2015.2479190

Yarman CE, Wang L, Yazici B, 2010. Passive synthetic aperture radar imaging with single frequency sources of opportunity. Proc IEEE Radar Conf, p.949-954. https://doi.org/10.1109/RADAR.2010.5494484